Power Electronic Systems
Laboratory

IEEE Transactions on Industrial Electronics, Vol. 61, No. 6, pp. 2960-2968, June 2014

A Novel Motor Topology for High-Speed Micro-Machining Applications

A. Tüysüz,
C. Zwyssig,
J. W. Kolar

Eidgenössische Technische Hochschule Zürich
Swiss Federal Institute of Technology Zurich

A Novel Motor Topology for High-Speed Micro-Machining Applications

Arda Tüysüz, *Student Member, IEEE*, Christof Zwyssig, *Member, IEEE*, and Johann W. Kolar, *Fellow, IEEE*

***Abstract*—In this paper, a novel motor topology (lateral stator machine) is proposed for various drilling applications where the space in the tool head is limited. The stator of the motor grows in one lateral direction, allowing for a compact direct drive design. Finite-element analysis (FEA) is carried out and the machine design is optimized for the specifications of a high-speed micro-machining spindle which is given as an example. The design procedure for those specifications is described in detail, where the torque is maximized while considering the space limitations and the loss constraints at the critical operating points. The construction of a lateral stator machine merged into a test bench is also described. The test bench is used for measuring the standstill torque of the machine in a configuration without bearings, such that only the electromagnetic torque is measured without any friction effects from the bearings. Moreover, the test bench can be modified to measure the no-load losses and separate the mechanical and electromagnetic components of it. Although described on a lateral stator machine, the measurement methodology of this paper can be applied to any electrical machine. Finally, measurement results are given and the design procedure is verified.**

***Index Terms*—AC machines, finite-elements method (FEM), high-speed machines, loss segregation, test bench, torque measurement.**

I. Introduction

HIGH-SPEED electrical drives have been a very popular research topic lately. Several electrical drives with speeds above 100 000 r/min and power levels from 100 W up to several kWs have been reported in literature. The driving force behind this is mainly the miniaturization trend in applications such as turbocompressors, gas turbines and machining spindles [1]. A 100 W, 500 000 r/min drive system is described in [1]. A 2 kW, 200 000 r/min machine is designed, optimized and tested in [2]. An overview of ultra-high-speed drive systems is given in [3]. The authors have analyzed the speed limits of high-speed electrical machines in [4].

The applications described above have one working point with a defined nominal speed and power. Hence, the motors are designed and optimized for this nominal speed and power, which is justified for typical high-speed applications such as turbo compressors. However, there are high-speed applications that have different torque and speed requirements. For example, the trend in micro-machining is toward smaller tools with high rotational speed and low torque requirements. On the other hand, the same spindle still has to be able to drive larger tools that require more torque at lower speeds. Such an application is micro-machining spindles for high-speed milling where tool diameters down to 0.1 mm are used which require almost zero torque at high-speeds [5], whereas the same spindles are also applied for thread cutting at low speeds where a high torque is needed. As further examples, new desktop machining centers are developed to process very small work pieces for the watch industry and for the manufacturing of dental crowns.

A further application with similar specifications is dental hand pieces. Currently, different hand pieces are used for different treatments that usually require low torque at high speeds and high torque at low speeds. Accordingly, there are activities to replace several hand pieces with low-speed motors and step-up gearboxes for distinct applications with a single direct-driven hand piece.

Other applications with similar requirements are hand power tools such as hand held sanding machines.

Slotless permanent magnet (PM) machines are commonly used in high-speed drives, mainly due to their simple and robust rotor construction and weak armature reaction which limits the rotor losses [6]. The torque of such a machine can only be increased by increasing the machine volume (for constant relative losses). This is, however, not possible in several applications that require a small size in order not to compromise the handling flexibility. For example, in desktop micro-machining centers the space for the milling spindle is very limited and the head size of a spindle limits the possible shapes of the work piece. Likewise, the head size of a dental hand piece influences the ergonomics for the patient and the dentist. Moreover, the maximum rotational speed of a machine is limited by the diameter and the length of the rotor due to mechanical stresses and rotor-dynamic constraints [4].

In [7] the authors have proposed a novel motor topology, the so-called lateral stator machine (LSM), to overcome the drawbacks of the present high-speed motors in space restricted applications. In that work, the lateral stator machine has been shown to allow for both high-torque low-speed and low-torque high-speed operation, with a small head size around the rotor. Two types of lateral stator machines are shown and they are analyzed using finite-element method (FEM) simulations due to the complicated geometry of the machine and the saturation in the iron parts. The specifications such as geometrical constraints, torque and losses are given and the geometrical parametrization of two different lateral stator machine topologies as well as

Manuscript received April 30, 2013; accepted June 19, 2013. Date of publication July 16, 2013; date of current version December 20, 2013.

A. Tüysüz and J. W. Kolar are with the Power Electronic Systems Laboratory, Swiss Federal Institute of Technology (ETH) Zurich, 8092 Zurich, Switzerland (e-mail: tuysuz@lem.ee.ethz.ch; kolar@lem.ee.ethz.ch).

C. Zwyssig is with Celeroton AG, 8005 Zurich, Switzerland (e-mail: christof.zwyssig@celeroton.com).

Color versions of one or more of the figures in this paper are available online at http://ieeexplore.ieee.org.

Digital Object Identifier 10.1109/TIE.2013.2273481

the modeling of the different loss components are described in detail. An exhaustive evaluation approach is adopted, meaning that all the possible machines in the given discrete parameter space are evaluated and then the best one is selected.

In [8] the authors described further considerations about building the lateral stator machine in detail. Moreover, they proposed a test bench which can evaluate the machines losses and torque, enabling a direct verification of the FEM simulations. This is done by designing two different test benches, one measuring the torque at standstill and the other measuring the no-load losses at higher speeds. In the standstill torque measurement setup, a bearingless configuration is designed, and the torque is measured on the stator side. This allows for the measurement of the electromagnetic torque only, without the bearing friction, which enables a direct verification of the FEM analysis. In the high-speed no-load loss measurement setup, deceleration tests are used to measure the total no-load losses. Moreover, a method for the separation of the mechanical losses from the electromagnetic losses is proposed.

In this paper, the highlights of [7] and [8] are briefly recaped by showing the proposed machine topologies and summarizing the modeling approach. The FEM models are enhanced to be slightly faster and also to cover the rotor losses which have been neglected in the previous work. For simpler construction, a new lateral stator machine with breadloaf shaped magnets on the rotor is analyzed, using a similar exhaustive approach, for slightly different specifications. The machine with the best performance is built and evaluated using the test bench described in [8]. Measurement results very well verify the design process.

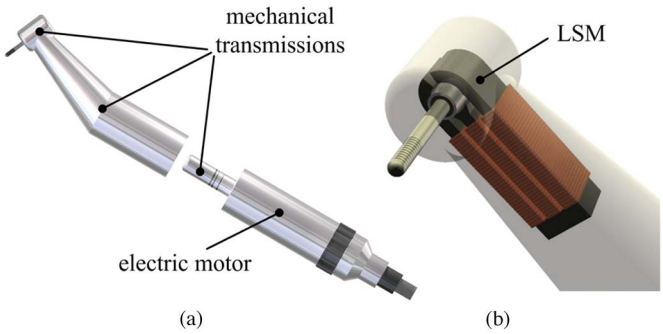

Fig. 1. (a) Dental hand piece with a low-speed motor and several stages of mechanical transmission. (b) A direct-driven dental hand piece using a LSM.

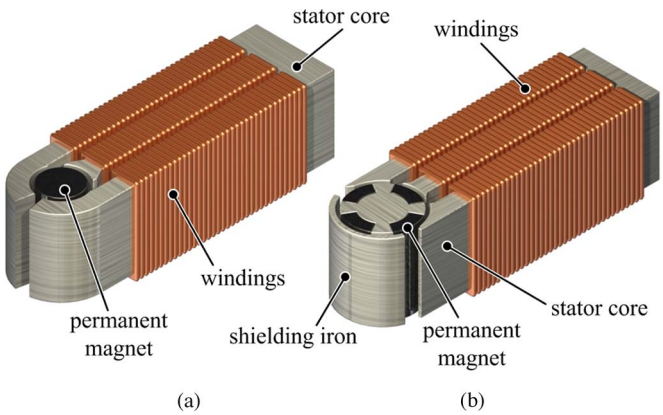

Fig. 2. Two novel lateral stator motor topologies presented in [7]: (a) motor with surrounding stator and (b) with section stator.

II. Lateral Stator Machine

A. Concept Description

To machine very small work pieces (e.g., for the watch industry) or for ergonomic reasons (e.g., for dental drills) the head of a machining spindle has a limited size, and the electrical motor is allowed to grow only in one lateral direction if a direct drive is to be used. In the example of the dental drills, the state-of-the-art is a low-speed motor (typically 40 000 r/min) placed in the middle of the hand piece where there is enough space, driving the drill at the tool head through several stages of mechanical transmission as shown in Fig. 1(a). The mechanical transmission stages introduce additional weight, acoustic noise and losses. A direct drive removes the need of mechanical transmission; however, the space in the tool head is too small for a machine that can generate the desired torque. In such a case, a lateral stator machine can be used as shown in Fig. 1(b) as it makes use of the space at the tool neck, which would otherwise not be used.

Two possible designs of the LSM are shown in Fig. 2. The machine shown in Fig. 2(a) is called the surrounding type LSM as the stator surrounds the rotor. It is derived from a three-phase, two-pole, three-slot electrical machine with double-layer concentrated windings. The shape of the stator is modified by moving the windings from the area where the space is limited. More space for the windings is gained by making the stator teeth longer and carrying the permanent magnet flux out of the confined space. The machine depicted in Fig. 2(b) is another type of LSM, which is called the section type LSM, as the lateral stator covers only a section of the rotor. This leads to a bigger rotor with higher number of poles. A rotor with four poles is used and a shielding iron is added to the design to guide the magnetic field of the rotor magnets which are not facing the stator teeth.

As the simulation results of [7] show, with the section type LSM, torque is increased compromising the simplicity of the rotor construction as there is more space for permanent magnets and the number of poles is increased. For that reason, in this work only the section type machine is considered. However, breadloaf shaped magnets are used instead of the arc shaped magnets for ease of construction and a one piece cobalt-iron shaft is used due to its mechanical strength instead of a laminated rotor core. The magnets are glued on the rotor core and grinded on the outer surface to have a precise outer diameter. Fig. 3 shows the LSM analyzed in this work, along with the geometrical parameters used to optimize the machine geometry.

Amorphous iron is chosen as the stator core material due to its lower losses compared to standard electrical steels and higher saturation flux density compared to ferrite materials. Sintered rare-earth magnets are used in the rotor for achieving a high torque density. A titanium sleeve is placed around the magnets to hold them together at high speeds as mentioned in [9] and [10]. The rotor is balanced dynamically as the final step of the rotor construction.

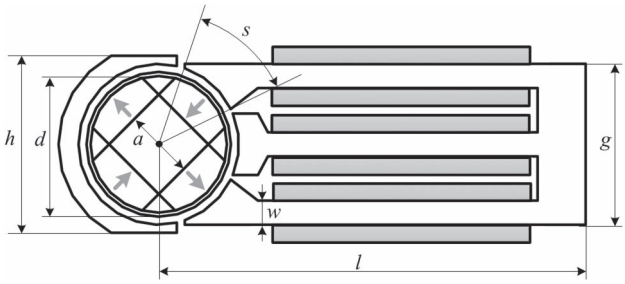

Fig. 3. Section type LSM analyzed in this paper and geometric parameters. Grey arrows show the magnetization direction of the permanent magnets.

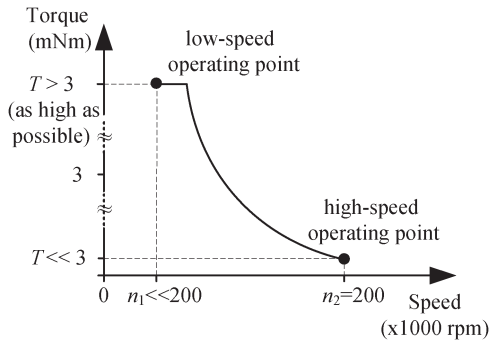

Fig. 4. Torque and speed requirements of a micro-machining application, as shown in [7].

B. Specifications

Trends in micro-machining applications show speeds from almost zero speed up to 200 000 r/min. The torque for the high-speed drilling and milling is very low and can be generated with negligible current, hence negligible copper losses. Therefore, only the no-load losses are relevant for the high-speed operation of the LSM. For the low-speed operation, a torque of 3 mNm is set as minimum and the goal is to maximize this torque for a given amount of copper losses. The speed dependent loss components such as the core losses or eddy current losses in the rotor can be neglected at low speeds, and only the copper losses are taken into account. Therefore, the operation of the LSM is simplified using two distinct operating points as shown in Fig. 4.

For a target application of dental drills, a preliminary thermal model is built for determining the loss limits assuming the use of the air spray of the hand piece for cooling of the machine. Setting the input air temperature to 25 °C and limiting the output air temperature at 37 °C (for ergonomic reasons) leads to maximum allowable losses of 2.4 W at the rated high-speed operating point of 200 000 r/min. On the other hand, as the maximum torque is usually applied only for a short time, considering the thermal capacitances and preliminary assumptions on the drive cycle, the maximum allowed copper losses are set to 6 W to avoid overheating of the windings.

III. Modeling and Optimization

Analytical models for evaluating the performance of PM machines with simple geometries are given in [11]. However, the approach presented in these works cannot be used here as the partial saturation of the stator, the stray flux and the torque ripple play a big role in determining the performance of the lateral stator machines; and these phenomena are not easy to model analytically on complex geometries. Therefore, FEM is used instead of an analytical modeling approach to find the machine that has the best performance.

TABLE I
Discretization of the Parameter Range: Independent Parameters, Parameters That Are Fixed According to Previous Analysis and Geometric Constraints

Symbol	Parameter name	Values
a	Shaft width	3.5, 4 (mm)
d	Rotor diameter	6.8 (mm)
g	Stator width	8 (mm)
h	Head width	8.8 (mm)
l	Stator length	10, 15, 20, 25 (mm)
s	Shoe span	40, 45 (deg)
w	Leg width	0.8, 1, 1.2, 1.4 (mm)
not shown	Machine depth (active length)	7.4 (mm)

For evaluating different possible machines and determining the effects of specific geometric parameters on the machine performance, the LSM geometry is parametrized as shown in Fig. 3, such that a unique set of parameters define a unique machine. These parameters are summarized in Table I.

Each of those parameter sets that represent a unique machine are evaluated using 2-D FEA. The advantage of such an exhaustive evaluation is its simplicity and certainty to the global optimum in the discretized parameter space. Furthermore, it yields data that are distributed over the entire parameter range, which allows for sensitivity analysis depending on any parameter and any performance criteria. The discretization steps shown in Table I are chosen relatively coarse, and the outcome of the analysis in [7] is taken into account while setting the parameter range (the rotor diameter is fixed to the largest possible value, the shielding iron is not parameterized to ensure enough shielding and the shoe span is not decreased below a certain level to maintain a smooth drive torque). However, after the verification of the design procedure, which is the main goal of this work, finer steps of discretization can be applied to a broader range of parameters for improving the design.

Two finite element simulations are carried out for each machine in the parameter range, one evaluating their performance in the low-speed and the other in high-speed operating point as shown in Fig. 4. First, a machine geometry is created by picking the geometrical parameters from the discrete parameter set. Then, depending on the machine geometry, the total winding area is calculated. Assuming a copper filling factor of 0.3, the peak current density is calculated according to the given copper loss value as described in Section III-A2. Three-phase, 120° phase shifted sinusoidal currents are assumed to be injected into the windings. Finally, the time-transient FEM model is solved for one electrical period. The torque is calculated by the virtual work principle and recorded. In the no-load simulation routine, the computations are repeated for zero winding current and the core losses in the lateral stator and the shielding iron as well as the eddy current losses in the rotor are calculated as described in Section III-A1, Section III-A3 and recorded.

A. Loss Models

1) Core Losses: The core losses are calculated using the method presented in [12] because it takes both nonsinusoidal and rotating flux effects into account, and it only needs the standard loss coefficients, which are generally provided by the manufacturers.

2) Copper Losses: The fundamental-frequency copper losses are the only significant loss components at low speeds as only sinusoidal currents are assumed. At the rated speed of 200 000 r/min, the drive current frequency is 6.66 kHz. At those frequencies and using copper conductors that are thin with respect to the skin depth, skin effect and proximity losses caused by the stray fields can be neglected and the total copper losses are calculated using (1), where $J_{\rm p}$ is the peak current density in the winding area, $\sigma_{\rm Cu}$ is the conductivity of copper and $k_{\rm f}$ is the copper filling factor. $A_{\rm w}$ represents the winding cross sectional area (i.e., area of one of the two adjacent rectangles between the stator legs in Fig. 3) and $l_{\rm w}$ represents the winding length (i.e., total length of the winding around one stator leg). Both $A_{\rm w}$ and $l_{\rm w}$ depend on the parameters given in Table I, and they are calculated separately for each independent parameter set

$$P_{Cu} = \frac{3 \cdot J_{\rm p}^2 \cdot A_{\rm w} \cdot l_{\rm w}}{2 \cdot k_{\rm f} \cdot \sigma_{\rm Cu}}. \tag{1}$$

3) Rotor Losses: Time and space harmonics of the air gap field induces eddy currents in the solid conductive bodies of the rotor in an electrical machine. To analyze those eddy currents accurately, a 3-D model is needed, as the eddy current problem is a 3-D problem by its nature. However, 3-D FEM simulations require much longer computational time than 2-D simulations. For that reason there have been efforts to approximate the eddy current losses using only 2-D simulations, like in [13]. This method depends on the assumption of uniform magnetic field density over a magnet body, and adjusts the electric resistivity of the permanent magnets according to their dimensions. The method is developed for rectangular permanent magnets.

In this paper, as the currents are neglected at the high-speed operating point, only the no-load eddy currents in the rotor are considered. Those eddy currents are induced because of the nonuniform air gap permeability. A 2-D field solution is used to calculate the eddy currents, neglecting the end resistances of the permanent magnets. This way, the calculation is kept simple; moreover, the calculated eddy currents are expected to be larger than the real eddy currents as the end resistances are neglected. This is considered to be an additional safety factor regarding the thermal considerations, as the cooling is poor in the rotor and overheating may demagnetize the permanent magnets.

For a solid conductor with a current source, the total current $I_{\rm t}$ is set and the FEM software computes the unknown source component $J_{\rm s}$ according to (2), where $A_{\rm c}$ is the width of the cross section of the conductor, $J_{\rm t}$ is the total current density and A is the magnetic vector potential

$$\int\int_{A_{\rm c}} \left(-\sigma \frac{dA}{dt} + J_{\rm s}\right) dA_{\rm c} = \int\int_{A_{\rm c}} J_{\rm t} dA_{\rm c} = I_{\rm t}. \tag{2}$$

To evaluate the eddy currents induced in the rotor, (2) is solved with the additional condition $I_{\rm t} = 0$ in the conducting bodies of the rotor. Finally, the eddy current losses are calculated using (3) where $P_{\rm eddy}$ is the eddy current loss in one conducting body whose conductivity is σ and volume is V

$$P_{\rm eddy} = \frac{1}{\sigma} \int_V J_{\rm t}^2 dV. \tag{3}$$

4) Bearing and Air Friction Losses: Air friction losses are calculated according to [11] as

$$P_{\rm air} = c_{\rm f} \cdot \pi \cdot \rho_{\rm air} \cdot \omega^3 \cdot r^4 \cdot z \tag{4}$$

where ρ_{air} is the density of air, ω is the angular speed, r is the radius and z is the length of the rotor and c_f is the friction coefficient. As the rotor diameter, the air gap clearance and the axial length of the rotor are all constants in this work, the air friction losses for all the machines in the considered parameter space are 0.3 W at 200 000 r/min.

Bearing friction losses are neglected at the initial stage as the heat conductivity from the bearings to the metallic machine housing is assumed to be high and the bearings losses are considered to be less likely to overheat the critical components of the motor such as the windings or the magnets.

B. Simulation Results

In Fig. 5, the results of the simulations are shown. The x-axis shows the electromagnetic no-load losses at the rated speed of 200 000 r/min. As the air friction losses are equal for all the machines in the design space, they are excluded from this plot to evaluate the effect of each parameter on the electromagnetic behavior of the machine clearly.

A careful observation of this figure gives insight into the electromagnetic behavior of the machine. For example, it can be seen that below a certain stator length, the winding area is small, limiting the torque. However, after a certain stator length, a longer stator does not necessarily always mean a higher torque. This is due to the increasing stray field with increasing stator length. In the parameter space analyzed here, increasing the width of the stator legs leads to higher torque and also higher no-load losses. Those results identify the leakage and the saturation of the legs as the two main limiting factors for the torque. Furthermore, decreasing the shoe span in all cases leads to increasing torque at the same no-load losses, due to the decreasing stray field.

From the machines that generate less no-load losses than the no-load loss limit of 2.4 W (which means 2.1 W electromagnetic no-load losses as the air friction losses are 0.3 W for all the machines), the one with the highest mean torque at 6 W copper losses is selected. According to the simulations, the selected machine has 1.67 W rotor losses, 0.42 W core losses and 0.3 W air friction losses. When driven with sinusoidal currents resulting in 6 W of copper losses, it generates the torque waveform shown in Fig. 6. Symmetric three-phase sinusoidal currents result in a high torque ripple due to the stator slotting and the partial saturation of the stator core. In [7] a current profiling approach is presented to reduce the torque ripple of an LSM at the expense of slightly increased copper losses.

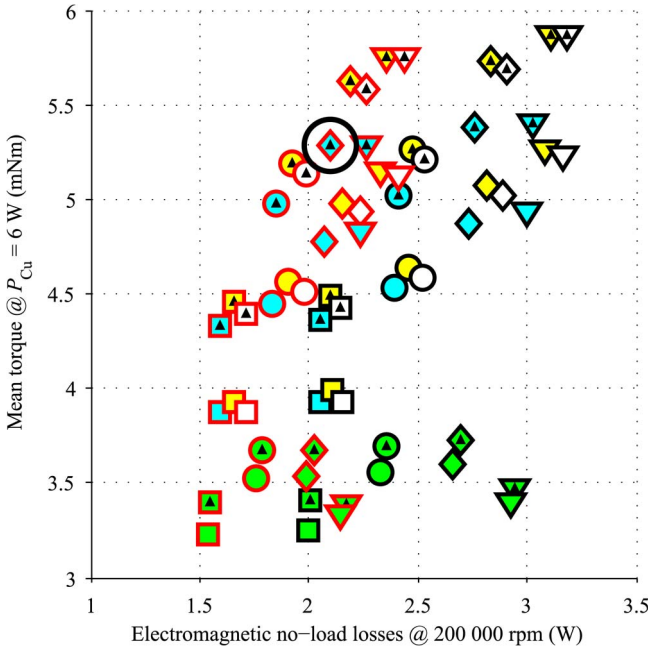

Fig. 5. Output of the simulation results. The marker border color denotes the shaft width a (red 3.5 mm, black 4 mm), the marker face color denotes the stator length l (green 10 mm, cyan 15 mm, yellow 20 mm, white 25 mm), the marker shape denotes the leg width w (square 0.8 mm, circle 1 mm, diamond 1.2 mm, triangle 1.4 mm) and the shoe span s is denoted by whether or not there is a black triangle in the center of the marker (triangle 40 deg., no triangle 45 deg.). The no-load loss limit is at 2.1 W and the selected machine is marked with a circle. The stator of this machine can be seen in Fig. 11(b).

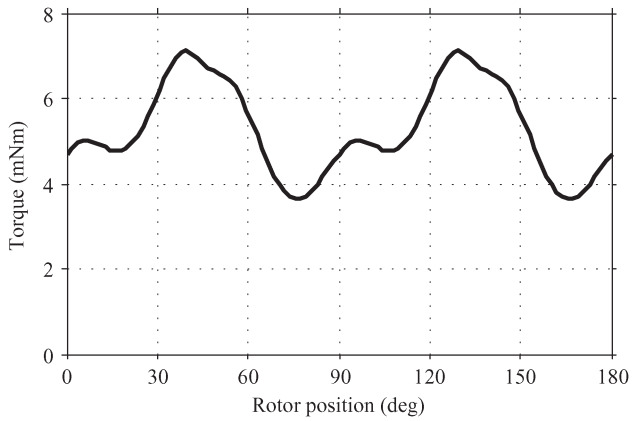

Fig. 6. Torque of the selected machine over the rotor position when driven with three-phase 120° phase shifted sinusoidal currents (peak 165 Ampere-turns) resulting in 6 W of copper losses. The average value of the torque is 5.28 mNm.

IV. Test Bench Design

After the best machine identified by the exhaustive simulations on the defined parameter range is built, a test bench is designed to evaluate its standstill torque and no-load losses at 200 000 r/min, to verify the FEM simulations. The first task of this test bench is to position the active components of the LSM (rotor, stator, shielding iron etc.) correctly with respect to each other, in other words, to keep the active components in their places during operation. This is achieved by the machine case consisting of a plastic chamber and the housing around it.

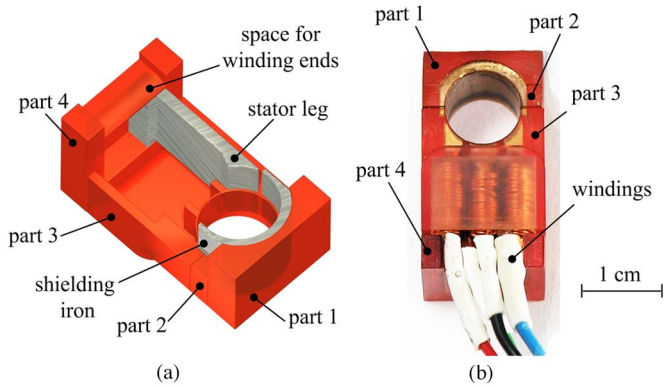

Fig. 7. (a) Illustration of the plastic chamber and the stator parts. For the sake of simplicity only half of the part 3, only one stator leg and and no windings are shown. (b) Photograph of plastic chamber with the lateral stator machine inside. The shielding iron and the lateral stator legs as well as the windings are visible through the plastic chamber.

The plastic chamber has be electrically nonconductive to ensure that no additional eddy current losses occur due to the rotor flux or the stray flux between the stator shoes. It also needs to be made of nonmagnetic material to maintain the magnetic air gap of the design. Furthermore, it has to be precisely machinable to be able to position the active parts correctly with respect to each other. Finally, it has to be mechanically strong enough to withstand the forces acting on the rotor and the stator parts. To fulfill these requirements, the pastic chamber is 3-D printed with stereolithography technique.

The plastic chamber consists of four pieces, helping the positioning of the lateral stator and the shielding iron. In Fig. 7(a), an illustration of the plastic chamber is shown. For better visibility, only the half section views of part 3 and part 2 of the plastic chamber and only one leg of the lateral stator are shown and the windings are omitted. It can be seen that part 3 of the plastic chamber is used for aligning the stator legs with respect to each other. The shielding iron is aligned with respect to the lateral stator legs by part 2. The air gap, which is formed by the circular faces of part 3 and part 2 does not change when part 1, part 4 and the iron parts are taken out. This allows for the separation of the no-load losses (see Section IV-B). The winding ends are taken out through the empty space on part 4 [8]. The photo of the plastic chamber as well as the lateral stator machine parts can be seen in Fig. 7(b).

The aluminum housing around the plastic chamber positions the plastic chamber (and hence the lateral stator and the shielding iron) with respect to the rotor. The aluminum parts are designed in a way that makes it is easy to take the plastic chamber out and put it back to its position precisely, without disassembling the bearings [8]. The LSM, plastic chamber and surrounding aluminum casing can be seen in Fig. 8.

A. Standstill Torque Measurement

The instantaneous torque of a PM machine depends on the rotor position and the stator currents as shown by (5), where T_{em} is the torque, i_1, i_2, i_3 are the three phase stator currents and ϕ is the angular position of the rotor. In [7] a plot of this function is shown for three-phase sinusoidal currents and

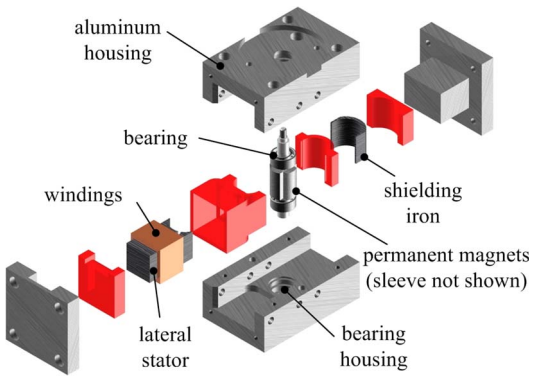

Fig. 8. LSM, plastic chamber, and surrounding housing in an exploded view.

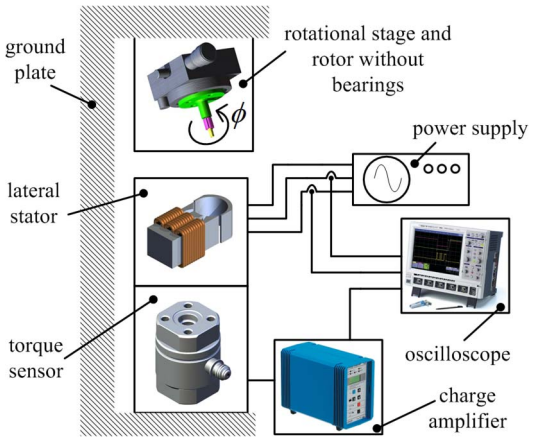

Fig. 9. Block diagram of the static torque measurement setup as shown in [8].

one rotor position of the LSM (with arc shaped magnets). The static torque measurement setup described here measures this function at standstill by measuring the stator reaction torque on a bearingless configuration

$$T_{\rm em} = f(i_1, i_2, i_3, \phi). \tag{5}$$

The static torque measurement setup is shown in Fig. 9 using a simplified diagram. In this setup, the rotor is fixed to a ground plate using a rotational positioning device, by which the rotor's angular position ϕ can be adjusted and fixed. The active parts of the stator (lateral stator, shielding iron and windings) which are held together by the plastic chamber and the aluminum housing are fixed to the ground plate via a piezoelectric torque transducer. The torque transducer is connected to an oscilloscope through a charge amplifier. Once the parts holding the rotor and stator are positioned such that rotor is centered in the stator bore - where it will be during normal operation with bearings installed - the stator reaction torque is recorded along with instantaneous stator currents for each rotor position [8]. Using this data, the torque function in (5) can be recreated.

The advantage of this configuration is the ability to measure the electromagnetic torque directly on a bearingless configuration, eliminating any disturbances introduced by the bearings. However, unlike familiar electrical measuring instruments, charges are processed when working with piezoelectric instruments and therefore static measurements without time limitations are essentially not possible. For that reason, this setup cannot measure the cogging torque of the LSM, as the rotor position is fixed during the measurements. The power supply used in this work applies purely sinusoidal voltages to the machine windings, consequently the effect of the inverter switching on the torque can not be directly evaluated either. However, the FEM simulations can be verified for different load conditions with high measurement accuracy, which is the main goal in this work.

B. No-Load Loss Measurement

The no-load losses in an electrical machine are mechanical losses (windage losses and bearing friction losses) and electromagnetic losses (rotor eddy current losses, stator core losses and proximity losses caused by the no-load stray flux in the windings). Using the no-load loss measurement setup described in this section, those losses can be measured and segregated.

In [2], the torque of an electrical machine is calculated by accelerating the machine and recording the angular position according to (6), where T_m is the total torque applied on the shaft, J_m is the inertia of the rotor, ω is the angular speed of the rotor and t is the time

$$T_{\rm m} = J_{\rm m}\frac{d\omega}{dt}. \tag{6}$$

Likewise, if the machine is first accelerated to a certain speed and then the drive power is cut off, the braking torque caused by the no-load losses can be calculated using the inertia and the deceleration of the machine. Using this deceleration test, the total no-load losses in a machine can be measured as a function of speed. However, different components of the total no-load losses cannot be separated [8].

In [14], a different method is proposed for measuring the loss of a permanent magnet machine. A dummy rotor, which has identical geometry as the original rotor is built, but with unmagnetized permanent magents. Using this dummy rotor, electromagnetic losses and the mechanical friction losses are separated. However, the bearing friction losses depend strictly on the preload, whose variation is hard to avoid or control while assembling the test bench or coupling the machine under test to a drive machine. This brings an uncertainty on the contribution of the bearing losses to the total no-load losses. Considering high-speed low-power machines, this uncertainty can not be neglected.

To separate the electromagnetic losses from the total no-load losses, a different method is proposed in [8]. This method consists of running deceleration tests with and without the stator.

In Fig. 10, the high-speed loss measurement setup is explained with a block diagram. A commercial ultra-high-speed electrical machine from Celeroton, CM-2-500, is used as a drive machine to accelerate the lateral stator machine to a desired speed. Then, the drive power is cut off, and the back EMF of the drive machine is recorded with an oscilloscope during deceleration. The speed is calculated using the back EMF. With the speed and inertia known, the total no-load losses of the drive machine and the lateral stator machine can be calculated. After

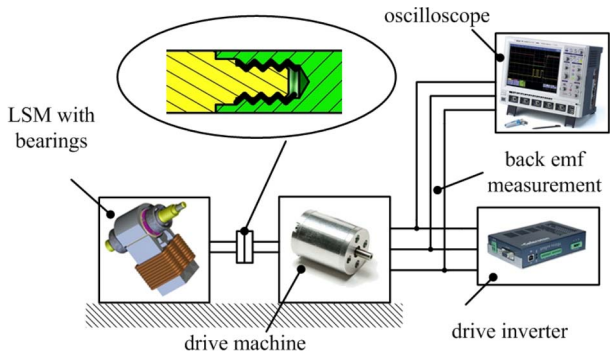

Fig. 10. Block diagram of the high-speed loss measurement setup as shown in [8]. The coupling between the drive machine and the lateral stator machine is zoomed in to show the coupling screw-thread as well as the alignment surfaces.

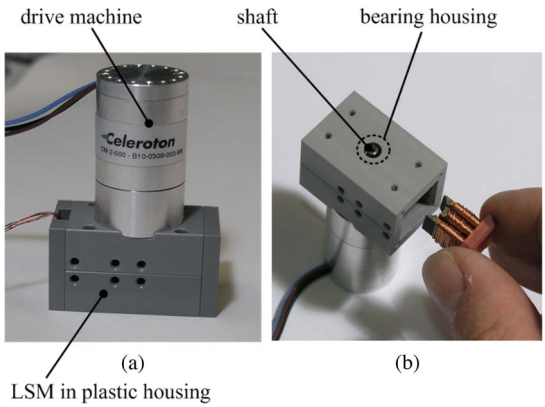

Fig. 11. (a) Photograph of the high-speed loss measurement setup with the drive motor and the LSM. (b) The stator and the shielding iron of the LSM can be taken out without disassembling the housing hence not changing the preload of the bearings [8].

running a deceleration test on this setup, the housing of the test bench is opened on both sides to take the stator and the shielding iron out. As the bearings are not disassembled, the preload and therefore the friction losses of the bearings do not change. The plastic chamber ensures that the air gap geometry stays the same; therefore the windage losses are also the same in the setups with and without the stator. The aluminum housing of the machine case is replaced by a plastic housing of the same geometry to avoid any additional eddy current losses when the stator and the shielding iron are taken out. A deceleration test on this setup gives the total no-load losses of the drive machine plus only the mechanical losses of the lateral stator machine. Accordingly, the electromagnetic losses of the lateral stator machine can be extracted. Furthermore, the proximity losses can be measured in a similar way, running deceleration tests with and without the windings around the stator. In Fig. 11, a photo of the high-speed loss measurement setup is shown [8].

In electrical machines, the critical speeds of the rotor can be a limiting factor on the maximum achievable speed. Therefore, the rotor dynamics of the test bench are analyzed using a 3-D FEM model. The critical speeds of the high-speed loss measurement setup are shown in Fig. 12. It can be seen that the first bending mode which limits the speed is out of the nominal speed range of the test bench (200 000 r/min); however, the first two rigid body modes occur below the rated speed.

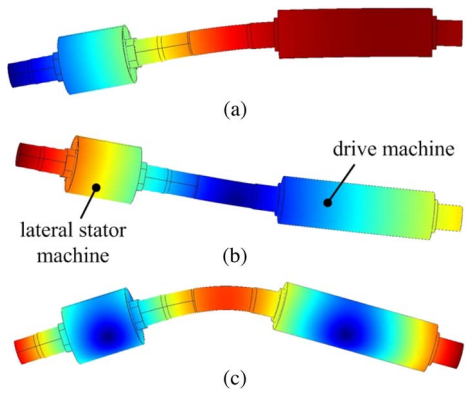

Fig. 12. Critical speeds of the high-speed loss measurement setup. (a) First rigid body mode at 2.27 kHz, 136 000 r/min; (b) second rigid body mode at 2.53 kHz, 152 000 r/min; and (c) first bending mode at 5.2 kHz, 312 000 r/min. Blue shows no displacement, red shows maximum displacement.

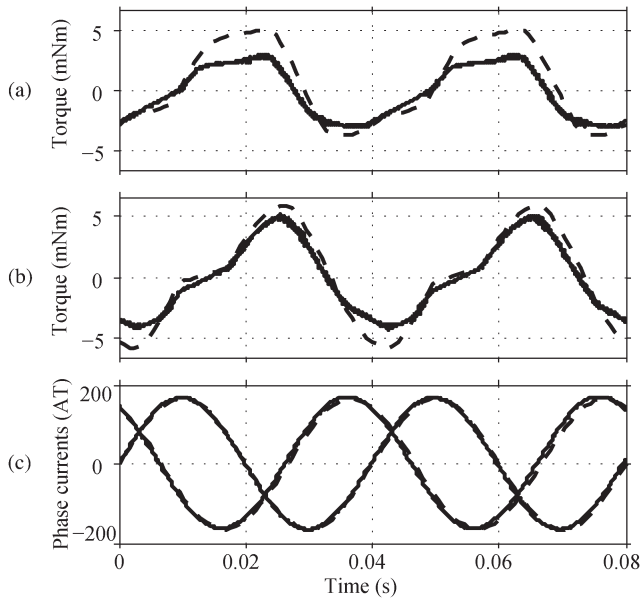

Fig. 13. Results of 2-D simulations and measurements for two different rotor positions (0 degrees and 20 degrees). (a), (b) Torque. (c) Total currents in machine windings in ampere-turns. Solid lines show measurements and dashed lines show simulation results.

Plastic o-rings are used with the high-speed ball bearings to limit the effect of the vibrations excited at those critical speeds. The o-rings also make the construction less sensitive to misalignments during coupling the drive machine to the machine under test.

V. Measurement Results

A. Standstill Torque Measurements

For the standstill torque measurement setup, the rotor is fixed at different angles and three phase, 120° phase shifted sinusoidal currents are pushed into the windings. The torque is recorded along with the currents. As a three phase Y-connected setup without star point connection is considered, only two phase currents are measured. Fig. 13 shows the results of this measurement and 2-D FEM simulation, for full load and two different rotor positions.

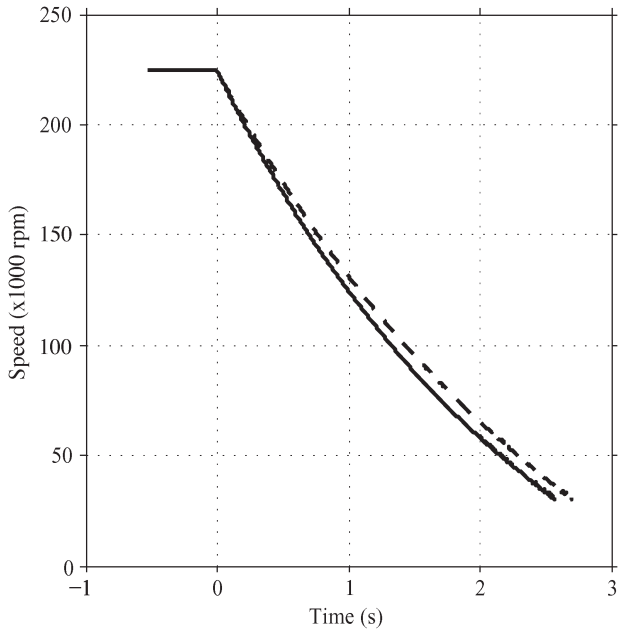

Fig. 14. Speed profiles calculated using the voltage measured at the terminals of the drive machine. Solid line shows the deceleration with and dashed line the shows the one without the lateral stator and the shielding iron of the LSM.

B. No-Load Loss Measurements

To measure the no-load losses, two deceleration tests are carried out, one with and one without the active parts of the LSM. The initial speed in these tests is set to 225 000 r/min, which is higher than the maximum speed requirement. The reason is to have measurement results over a broader range, considering some data loss due to filtering and smoothing at the post-processing stage.

The back EMF of the drive machine is measured across two of its terminals and recorded during deceleration. A decaying sinusoidal curve is fit on the measured data and the frequency and hence the speed is obtained. Speed profiles during the two deceleration tests are plotted in Fig. 14.

The losses for the two deceleration test are calculated using the calculated speed profiles and (6). Their difference gives the electromagnetic no-load losses of the LSM, and is shown in Fig. 15. It can be seen on the same figure that the 2-D FEM simulations resulted in a much higher no-load loss compared to the measurements. To investigate this difference further, a 3-D model of the prototype machine was built and simulated for three different speeds. The results from the 3-D models agree with the measurements better. This verifies the approach of using 2-D models and considering the pessimistic loss calculations as an additional safety factor. However, as the difference to the measurement is considerably high, methods like the one described in [13] will be considered in the future work to get more accurate results from 2-D models.

The measured back EMF at 200 000 r/min of the LSM is shown in Fig. 16. The asymmetric properties of the LSM can be seen once more as the back EMF of the middle phase is different than that of the two outer phases. For this prototype the number of stator winding turns is 33, leading to a phase inductance of 27 μH for the outer phases and 36 μH for the middle phase. The phase resistance is 0.3 Ω. In the first prototype the copper

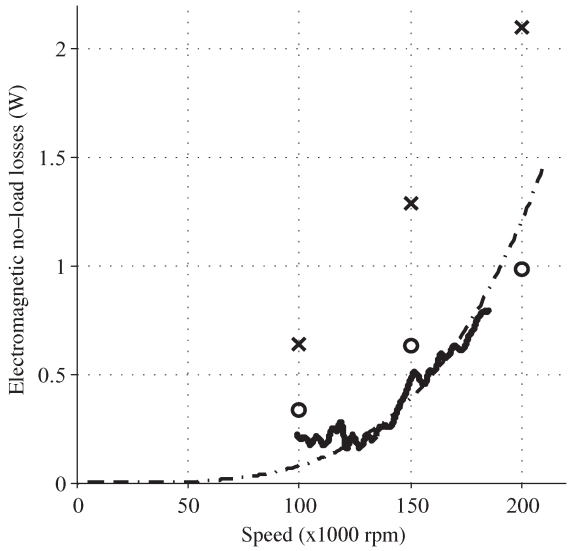

Fig. 15. Electromagnetic no-load losses of the LSM. 2-D simulation results (x). 3-D simulation results (o). Solid line shows the difference of two no-load loss measurements, one with and one without the stator and the shielding iron of the LSM. Dashed line shows the fitted curve. It can be seen that the 3-D simulations predict the losses better than the 2-D simulations.

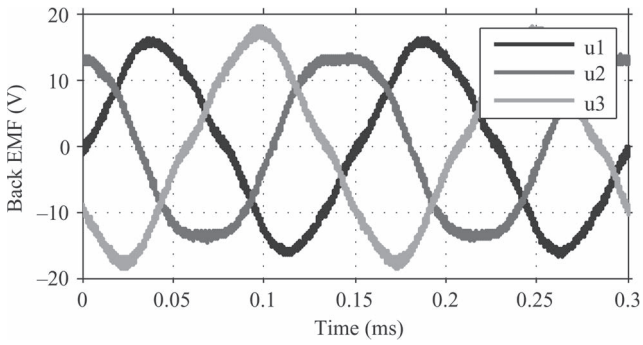

Fig. 16. Back EMF of the LSM prototype with 33 windings. u1, u2 and u3 are measured on the machine terminals with respect to the star point. u2 is the middle phase.

filling factor k_f is lower than the assumed value $k_f = 0.3$ due to the hand wound windings, resulting in higher stator resistance. However, this prototype can be used without any problems for the verification of the design process.

VI. Conclusion

In drilling and machining applications with a wide speed and torque range where the space in the head of the tool is limited and mechanical transmission should be avoided, state-of-the-art high-speed permanent magnet motors cannot supply the torque required at low speeds. Therefore, a novel motor concept that fits in the head of the tool by extending the stator to one lateral side is described in this paper.

Due to the complex geometry of the machine, parametric FEM models are used, allowing the selection of an ideal machine concerning torque and loss characteristics. A machining spindle was chosen as an example target application, and the simulations identified the ideal machine that can supply 5.4 mNm torque at low speeds and has only 2.1 W of no-load losses at 200 000 r/min.

The LSM is merged into a test bench whose design is described in detail. Using this test bench, the torque of the machine can be measured without the bearing friction; therefore the FEM analysis can be directly verified. In a modified test setup, the total no-load losses including the electromagnetic and mechanical losses of the machine can be measured and segregated. Measurements verify the machine design procedure.

Future work includes modification of the 2-D rotor loss models such that they account for 3-D effects for more accurate rotor loss calculations. More detailed thermal models and temperature rise tests will be used to verify the assumed loss limits for the given example application. Long lifetime tests will be carried out to check how the bearings behave under the asymmetric forces acting on the rotor, which is an intrinsic property of the LSM.

ACKNOWLEDGMENT

The authors would like to thank Inspire AG for providing the torque transducer and the charge amplifier, Vacuumschmelze GmbH & Co. KG for supplying the rotor steel material as well as the permanent magnets, and Metglas Inc. for supplying the stator core material.

REFERENCES

[1] C. Zwyssig, S. D. Round, and J. W. Kolar, "An ultrahigh-speed, low power electrical drive system," *IEEE Trans. Ind. Electron.*, vol. 55, no. 2, pp. 577–585, Feb. 2008.

[2] P. D. Pfister and Y. Perriard, "Very-high-speed slotless permanent-magnet motors: Analytical modeling, optimization, design, and torque measurement methods," *IEEE Trans. Ind. Electron.*, vol. 57, no. 1, pp. 296–303, Jan. 2010.

[3] M. A. Rahman, A. Chiba, and T. Fukao, "Super high speed electrical machines—Summary," in *Proc. IEEE Power Eng. Soc. Gen. Meeting*, Jun. 2004, vol. 2, pp. 1272–1275.

[4] A. Borisavljevic, H. Polinder, and J. A. Ferreira, "On the speed limits of permanent-magnet machines," *IEEE Trans. Ind. Electron.*, vol. 57, no. 1, pp. 220–227, Jan. 2010.

[5] M. H. Kimman, H. H. Langen, J. van Eijk, and R. M. Schmidt, "Design and realization of a miniature spindle test setup with active magnetic bearing," in *Proc. IEEE/ASME Int. Conf. Adv. Intell. Mechatron.*, Sep. 2007, pp. 1–6.

[6] N. Bianchi, S. Bolognani, and F. Luise, "Potentials and limits of high-speed PM motors," *IEEE Trans. Ind. Appl.*, vol. 40, no. 6, pp. 1570–1578, Nov./Dec. 2004.

[7] A. Tüysüz, A. Looser, C. Zwyssig, and J. W. Kolar, "Novel miniature motors with lateral stator for a wide torque and speed range," in *Proc. 36th Annu. Conf. IEEE Ind. Electron. Soc.*, Nov. 2010, pp. 1741–1747.

[8] A. Tüysüz, D. Koller, A. Looser, and J. W. Kolar, "Design of a test bench for a lateral stator electrical machine," in *Proc. 37th Annu. Conf. IEEE Ind. Electron. Soc.*, Nov. 2011, pp. 1801–1806.

[9] W. Li, H. Qiu, X. Zhang, J. Cao, and R. Yi, "Analyses on electromagnetic and temperature field of super high speed permanent magnet generator with different material sleeves," *IEEE Trans. Ind. Electron.*, vol. 61, no. 6, pp. 3056–3063, Jun. 2014.

[10] J. Ikaheimo, J. Kolehmainen, T. Kansakangas, V. Kivela, and R. Moghaddam, "Synchronous high-speed reluctance machine with novel rotor construction," *IEEE Trans. Ind. Electron.*, vol. 61, no. 6, pp. 2969–2975, Jun. 2014.

[11] J. Luomi, C. Zwyssig, A. Looser, and J. W. Kolar, "Efficiency optimization of a 100 W 500 000 r/min permanent-magnet machine including air-friction losses," *IEEE Trans. Ind. Appl.*, vol. 45, no. 4, pp. 1368–1377, Jul./Aug. 2009.

[12] D. Lin, P. Zhou, W. N. Fu, Z. Badics, and Z. J. Cendes, "A dynamic core loss model for soft ferromagnetic and power ferrite materials in transient finite element analysis," *IEEE Trans. Magn.*, vol. 40, no. 2, pp. 1318–1321, Mar. 2004.

[13] S. Ruoho, T. Santa-Nokki, J. Kolehmainen, and A. Arkkio, "Modeling magnet length in 2-D finite-element analysis of electric machines," *IEEE Trans. Magn.*, vol. 45, no. 8, pp. 3114–3120, Aug. 2009.

[14] A. S. Nagorny, "A simple and accurate method for the experimental performance evaluation of high speed sensorless brushless DC motors," in *Proc. Electr. Mach. Drives Conf.*, May 2009, pp. 916–921.

Arda Tüysüz (S'10) received the B.Sc. degree in electrical engineering from Istanbul Technical University, Istanbul, Turkey, in 2006 and the M.Sc. degree from RWTH Aachen University, Aachen, Germany, in 2009. Since June 2009, he has been with the Power Electronic Systems Laboratory of the Swiss Federal Institute of Technology (ETH) Zurich, Zurich, Switzerland, as a Ph.D. student.

His Ph.D. research focuses on novel electrical machine topologies for high-speed drives and self-sensing control of high-speed electrical machines.

Christof Zwyssig (M'10) received the M.Sc. and Ph.D. degrees in electrical engineering from the Swiss Federal Institute of Technology Zurich, Switzerland, in 2004 and 2008, respectively.

He studied power electronics, machines, and magnetic bearings and was engaged in research on high-speed electrical drive systems and their power electronics. Since January 2009, he has been with Celeroton AG, Zurich, Switzerland, a spin-off company in the area of high-speed electrical drive systems, of which he is a co-founder.

Johann W. Kolar (M'89–SM'04–F'10) received the M.Sc. and Ph.D. degrees (*summa cum laude*/*promotio sub auspiciis praesidentis rei publicae*) from Vienna University of Technology, Vienna, Austria.

Since February 1, 2001, he has been a Professor and the Head of the Power Electronic Systems Laboratory, Swiss Federal Institute of Technology (ETH) Zurich, Switzerland. He has proposed numerous novel PWM converter topologies, and modulation and control concepts, e.g., the Vienna Rectifier, the Swiss Rectifier, and the Three-Phase AC-AC Sparse Matrix Converter. He has published over 550 scientific papers in international journals and conference proceedings and filed more than 110 patents.